J. Fluid Mech. (2010), *vol.* 662, *pp.* 269–287.
doi:10.1017/S0022112010003198

An experimental study of slip considering the effects of non-uniform colloidal tracer distributions

HAIFENG LI AND MINAMI YODA†

G. W. Woodruff School of Mechanical Engineering, Georgia Institute of Technology, Atlanta, GA 30332-0405, USA

(Received 17 November 2009; revised 31 May 2010; accepted 9 June 2010; first published online 17 September 2010)

Various studies have suggested that the no-slip condition may not hold for Newtonian liquids flowing over (for the most part) non-wetting surfaces. This paper describes an experimental study of steady Poiseuille flow at various Reynolds numbers up to 0.12 of four different aqueous monovalent electrolyte solutions through naturally hydrophilic and hydrophobically coated fused-silica channels with a depth of 33 μm. The slip lengths for these flows were estimated using a local method based on a new particle velocimetry technique that determines velocities at three different wall-normal distances within the first 400 nm next to the wall. These results are corrected using direct measurements of the near-wall particle distribution, which is highly non-uniform as expected due to repulsive electric double-layer interactions between the 100 nm tracer particles and the wall. In all cases, the slip lengths were not more than 23 nm and for all but one case, zero within their uncertainties. As illustrated here, the standard assumption of uniformly distributed tracers can significantly increase slip length estimates obtained using local methods and near-wall velocity data.

Key words: micro-/nano-fluid dynamics

1. Introduction

The 'no-slip' condition, stating that the tangential component of velocity is continuous across a material boundary between a fluid and a solid, has been the accepted boundary condition at solid–fluid interfaces for nearly a century. As noted by Batchelor (1967), 'the absence of slip at a rigid wall is now amply confirmed by direct observation and by the correctness of its many consequences under normal conditions'. Nevertheless, the no-slip condition is a special case of the partial-slip condition proposed by Navier (1823), which states that the tangential component of velocity $u(z)$ at the boundary (i.e. wall) is proportional to the shear stress at the boundary: $u(0) = b(\partial u/\partial z)|_{z=0}$, where b is the slip length and z denotes the coordinate normal to and measured from the interface, or wall. For the no-slip condition, $b = 0$, based on the assumption that the fluid and solid molecules have similar behaviour.

Over the past decade, a number of experimental, numerical and theoretical studies have suggested that the no-slip condition may break down for Newtonian liquids flowing past non-wetting (e.g. hydrophobic) and, in some cases, wetting (e.g. hydrophilic) surfaces. Recent reviews of this literature can be found in Lauga, Brenner

† Email address for correspondence: minami@gatech.edu

& Stone (2005), which discusses the dependence of slip on various physical parameters, Neto *et al.* (2005), which focuses on experimental studies of slip for Newtonian liquids, Bocquet & Barrat (2007), which focuses on theoretical studies of slip mechanisms, and Maccarini (2007), which focuses on how slip may be due to changes in the molecular structure of the layer of water in direct contact with the solid wall. Experimental studies of slip use either 'local' or 'indirect' methods to determine slip length. The indirect methods estimate b by assuming that the slip length has a particular effect on a quantity such as the flow rate (Cheng & Giordano 2002; Choi, Westin & Breuer 2003), the draining or viscous force in a narrow gap (Zhu & Granick 2001; Bonaccurso, Kappl & Butt 2002; Cho, Law & Rieutord 2004; Henry *et al.* 2004; Honig & Ducker 2007; Cottin-Bizonne *et al.* 2008) or diffusion times over a known distance (Joly, Ybert & Bocquet 2006).

The local methods, on the other hand, directly estimate b by extrapolating the tangential velocity component profile $u(z)$ near the wall where z is the wall-normal coordinate. A direct estimate of slip length should, in theory, be more accurate than that obtained with an indirect method. The velocity profile near the wall has been measured with a variety of velocimetry techniques, including microscale particle-image velocimetry (μPIV), evanescent wave-based PIV and particle-tracking velocimetry (PTV), total internal reflection fluorescence recovery after photobleaching (TIR-FRAP) and fluorescence-correlation spectroscopy (FCS). In all of these techniques, the local fluid velocity is determined by determining the displacement of either a particle or molecular tracer over a known time interval under the assumption that the tracer velocity is the fluid velocity. Here, PIV refers to techniques that determine the (average) displacement of (groups of) particle tracers using cross-correlation-based approaches, while PTV refers to techniques that obtain displacements of individual particles from the positions of the particle centres.

Tretheway & Meinhart (2002), who extrapolated μPIV velocity profiles in Poiseuille flow through glass microchannels coated with a self-assembled monolayer (SAM) of octadecyltrichlorosilane (OTS), reported slip lengths of almost 1 μm at shear rates $\dot{\gamma}$ up to $O(10^2\ \mathrm{s}^{-1})$, and subsequently attributed these large values to apparent slip due to the presence of a gas layer between the fluid and the wall (Tretheway & Meinhart 2004). Joseph & Tabeling (2005), who also measured velocities at different distances from the wall in Poiseuille flow using μPIV, obtained slip lengths over hydrophobically coated surfaces that were less than their measurement uncertainty of 100 nm for $\dot{\gamma} \leqslant 450\ \mathrm{s}^{-1}$. Huang, Guasto & Breuer (2006), who used total internal reflection velocimetry (TIRV) with a statistical particle-tracking approach (Breedveld *et al.* 1998; Guasto, Huang & Breuer 2006), reported slip length values up to 96 nm at shear rates as great as $1.8 \times 10^3\ \mathrm{s}^{-1}$. Lasne *et al.* (2008) measured velocities in the gap between stationary and sinusoidally oscillating flat plates for $\dot{\gamma} < 2.3 \times 10^3\ \mathrm{s}^{-1}$ by illuminating 20–40 nm fluorescent particles and fluorescent molecules with evanescent waves, and reported $b = 45$ nm for hydrophobically coated glass surfaces.

Pit, Hervet & Leger (2000) reported slip lengths as great as 400 nm for hexadecane flowing over sapphire surfaces hydrophobically coated with an OTS SAM for shear rates up to $2 \times 10^3\ \mathrm{s}^{-1}$ using the TIR-FRAP method. More recently, Schmatko, Hervet & Leger (2005), who used TIR-FRAP to compare slip lengths for rotating Couette flow over sapphire surfaces of varying wettability for shear rates up to $5 \times 10^3\ \mathrm{s}^{-1}$, obtained slip lengths as great as 350 nm for hexadecane and 150 nm for squalane. Finally, a number of groups have used FCS to estimate slip lengths of aqueous electrolyte solutions over silicate glass surfaces. Lumma *et al.* (2003) reported slip lengths up to 1 μm for $\dot{\gamma} \leqslant O(10^1\ \mathrm{s}^{-1})$. Joly *et al.* (2006) found much smaller slip

lengths of 18 nm for borosilicate and BK7 borosilicate crown glass surfaces at much higher shear rates of $\dot{\gamma} \leqslant 5 \times 10^3$ s^{-1}. Vinogradova *et al.* (2009) reported slip lengths as great as 80–100 nm for a borosilicate glass surface treated with trimethylchlorosilane to make a hydrophobic surface for $\dot{\gamma} \leqslant 3 \times 10^3$ s^{-1}.

Despite the large number of studies that report non-zero values of b, there does not appear to be a consensus at present on the conditions under which slip occurs, nor is there agreement on the fundamental mechanisms that lead to slip. The breakdown of the no-slip condition has been attributed to the following factors, among others:

(i) surface wettability, with the majority of experimental studies reporting that slip length increases as wettability decreases with little, if any evidence of slip for wetting surfaces;

(ii) shear rate, with most studies reporting that the slip length first increases as $\dot{\gamma}$ increases beyond a minimum critical value (Thompson & Troian 1997; Choi *et al.* 2003; Neto, Craig & Williams 2003), then approaches a limiting value at high shear rates;

(iii) nanobubbles, or the formation of a stable thin layer of gas (either dissolved gases or vapour) at the surface (Tretheway & Meinhart 2004);

(iv) surface roughness, with numerical and experimental studies reporting that an increase in surface roughness can either reduce (Zhu & Granick 2002; Priezjev & Troian 2006; Schmatko, Hervet & Leger 2006) or enhance (Bonaccurso, Butt & Craig 2003; Sbragaglia *et al.* 2006) slip.

In summary, the slip lengths for Newtonian liquids obtained from local methods vary by more than two orders of magnitude, ranging from a few nm to about 1 μm, and there is little agreement about the conditions under which slip occurs. The wide variation in b is due in part to the experimental difficulties in accurately measuring slip lengths. Since slip lengths are extrapolated from near-wall velocity data, accurate estimates of b require spatially well-resolved measurements of the velocity profile $u(z)$ near the wall, and accurate estimates of the tangential velocity component u and its wall-normal position z. The accuracy in z should, if possible, be less than the slip length itself.

Evanescent wave-based techniques are uniquely suited to near-wall velocity measurements because the illumination, which is generated by the total internal reflection (TIR) of light at a planar refractive-index interface, only exists near the interface. The boundary condition on Maxwell's equations requires that the tangential component of the electromagnetic field must be continuous across the interface, and hence the evanescent wave, corresponding to the portion of the electromagnetic field with complex wavenumbers, is not reflected, but is instead transmitted into the lower index medium, propagating parallel to the interface. The intensity of this evanescent wave I decays exponentially with distance normal to the interface z due to its complex wavenumber. The length scale for this exponential decay, the intensity-based penetration depth z_p, is a function of the wavelength of the illumination, the angle of incidence of the light on the interface (note that this must exceed the critical angle), and the refractive indices of the two media.

For blue light undergoing TIR at a glass–water interface at an angle of incidence of 70°, $z_p \approx 100$ nm. Evanescent waves can, therefore, be used to interrogate the first few hundred nanometres next to the wall. (The outer limit of this region is usually determined by the noise levels and sensitivity of the imaging system.) Moreover, the exponential decay of the illumination suggests that tracers near the wall should be brighter than those farther from the wall. In theory, the z-position of each tracer can then be determined from its image assuming that the particle image intensity, I_p, has

the same exponential decay as that of the illumination:

$$I_p(z) = I_p^0 \exp\left\{\frac{z-a}{z_p}\right\}, \tag{1.1}$$

where I_p^0 is the intensity of particles of radius a touching the wall, i.e. with centres at $z = a$. Because evanescent waves are generated at the interface, the particle image intensities are automatically measured with respect to the wall. And, in contrast with the volume illumination used for μPIV, the non-uniform exponentially decaying nature of evanescent-wave illumination makes it possible to quantify the z-positions of the tracers and their distribution in z in the near-wall region.

Since I_p^0 has significant variations in practice, with standard deviations as great as 9 % for $a = 50$ nm particles due to variations in particle properties and imaging noise, however, Li, Sadr & Yoda (2006) developed an evanescent wave-based particle velocimetry technique that instead divides, or bins, the images of colloidal particles illuminated by evanescent waves based on their maximum grey-scale value into a few sublayers spanning a range of different z-positions for 50 nm $\leqslant z \leqslant$ 400 nm. In their studies of the Poiseuille flow of aqueous electrolyte solutions through fused-silica microchannels, they inverted (1.1) to estimate the z-positions of these particles, and showed that these $a = 50$ nm polystyrene (PS) particles have a highly non-uniform distribution, with a particle 'depletion layer', where there are almost no particles within a diameter of the wall, due in part to repulsive electric double layer (EDL) interactions between the negatively charged sulphate-terminated particles and the negatively charged fused-silica wall (Li & Yoda 2008). These non-uniform distributions were qualitatively similar to those measured by Kanda *et al.* (2007) with a similar technique. After correcting their velocity data in their three sublayers for the non-uniform tracer distribution, a linear curve-fit of these velocity data gave estimates of the shear rate in creeping Poiseuille flow that were within 5 % of analytical predictions.

In the previous study, a linear function was curve-fitted to the three velocity data points corresponding to the results for the three sublayers and the origin, since it was assumed, based on previous slip studies, that $b = 0$ for the flow through these naturally hydrophilic channels. In this paper, the technique of Li & Yoda (2008), which we rename multi-layer nano-particle tracking velocimetry (MnPTV), is used to study Poiseuille flow through hydrophilic and hydrophobic channels under conditions that are otherwise similar within experimental limitations. After determining near-wall particle distributions and correcting the velocity results in each sublayer to account for the effects of non-uniform particle distribution, the errors in both u and z are estimated, and used to determine the error in the slip length values obtained from linear regression of these data. The implications of assuming uniformly distributed tracers – the standard assumption made in most tracer-based techniques – on slip length and slip studies are also discussed.

The remainder of this paper is organized as follows. The experiments on Poiseuille flow through both hydrophilic and hydrophobic microchannels and MnPTV processing are detailed in § 2. Section 3 presents and discusses the particle distributions, the velocities after correction, the slip lengths obtained from linear regression of these velocities and the uncertainties in these results. The conclusions are summarized in § 4.

2. Experimental details

Steady creeping Poiseuille flow was studied through fused-silica microchannels of roughly trapezoidal cross-section with nominal cross-sectional dimensions of

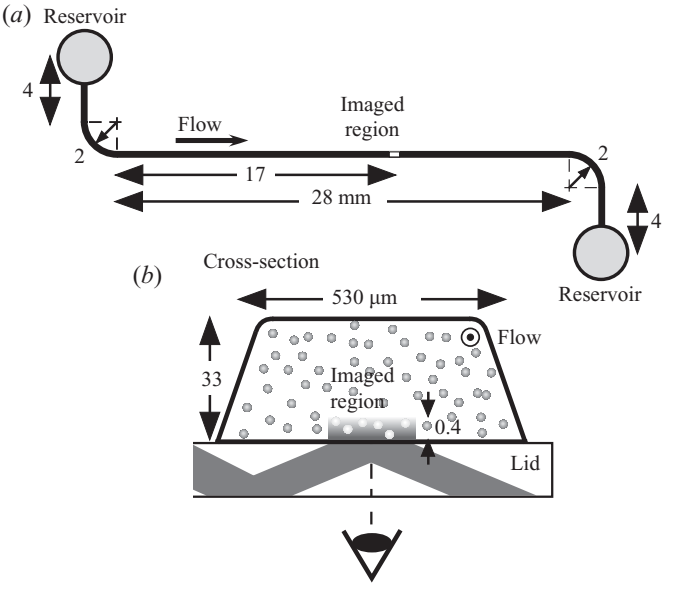

FIGURE 1. (*a*) Top and (*b*) cross-sectional views of microchannel. The dimensions in (*a*) and (*b*) are in millimetre and micrometre, respectively.

$H = 33\,\mu$m (depth) and 530 μm (width at the channel half-depth), and an overall length of 42.3 mm (figure 1). Trapezoidal trenches were first etched into a 100 mm × 100 mm × 2.2 mm fused-silica wafer (Telic Company) using standard photolithography and chemical wet-etching procedures; up to eight channels were etched onto a single wafer with dark-field photomasks of the same geometry. The trenches were then fused to 50.8 mm × 25.4 mm × 1 mm thick fused-silica substrates (Esco Products R320110) with an r.m.s. surface roughness of 3 nm (according to the manufacturer) by heating the wafer and substrate to about 1100 °C. Finally, the ends of the channel were attached through 1 mm diameter holes ultrasonically drilled in the substrate to reservoirs consisting of segments of glass tubing with an inner diameter of 4 mm and an axial extent of 12 mm.

Both 'bare' and unmodified, naturally hydrophilic fused-silica microchannels and hydrophobically coated fused-silica microchannels were studied. The hydrophilic fused-silica walls were made hydrophobic by coating the microchannel with an OTS SAM about 2 nm in thickness (Yi *et al.* 2008, among others). Given that the hydrophilic and hydrophobically coated channels studied here were from the same wafer and wet-etched under identical conditions, any variations in the geometry between the two types of channels are determined by variations in the wet-etch process itself, versus the thickness of the SAM layer. The contact angle of water on a fused-silica substrate from the same batch as that used for the microchannels coated using this procedure was $100 \pm 4.1\,^{\circ}$, as measured with a contact-angle goniometer (Ramé-hart Instrument Co. model 200), verifying that the microchannel walls after coating were indeed hydrophobic. The contact angle of water on an uncoated fused-silica substrate, measured using the same procedure, was $28 \pm 4\,^{\circ}$. Further details are given in Li (2008) and Li & Yoda (2008).

Four different monovalent aqueous electrolyte solutions were used as working fluids to investigate if either the ionic strength or pH of the working fluid affected slip lengths. Ammonium bicarbonate (NH_4HCO_3) and ammonium acetate

(CH_3COONH_4) solutions at molar salt concentrations $C = 2$ and 10 mM were chosen because of the buffering capability of the ammonium ion. The pH values of the 2 and 10 mM NH_4HCO_3 solutions were 7.6 and 7.8, respectively, while those of the 2 and 10 mM CH_3COONH_4 solutions were 6.2 and 6.6, respectively. All pH values were measured with a pH meter (Oakton Instruments pH 11) at the ambient temperature, which varied between 19.1 and 20.1 °C. The NH_4HCO_3 solutions were prepared from nanopure water and analytical grade NH_4HCO_3 salt (Acros Organics 370930250), while the CH_3COONH_4 solutions were prepared by diluting a 7.5 M CH_3COONH_4 stock solution (MP Biomedicals Inc. 198759) with nanopure water to the appropriate concentration. In all cases, the solutions were then filtered through a 200 nm pore size syringe filter (Whatman Puradisc) and seeded with radius $a = 50$ nm (with a standard deviation of 6 % according to the manufacturer) polystyrene spheres (Invitrogen FluoSpheres f-8888) that were labelled with the fluorophore Bodipy FL (Invitrogen) with absorption and emission maxima at 505 and 515 nm, respectively. The volume fraction of the tracers $\phi = 20$ ppm, corresponding to a particle number density $c = 4.4 \times 10^{16}$ m^{-3}. Finally, the seeded fluid was sonicated for about 20 min to minimize particle aggregation, then degassed by placing the solution in a vacuum chamber at a gauge pressure of −0.9 bar for 30 min. Before each experimental run, the microchannel was cleaned by driving 1 M NaOH, followed by nanopure water, acetone, again nanopure water and finally some of the working fluid (without particles), through the channel by applying a vacuum to the downstream reservoir.

The Poiseuille flows were driven hydrostatically by attaching the upstream reservoir to a fluid-filled reservoir whose height was adjusted to control the pressure gradient. The height difference between the container and downstream reservoir free surfaces (and hence the pressure gradient driving the flow) varied by less than 1 % in all cases during a single experimental run. Near-wall velocity data were obtained at six different pressure gradients $dp/dx = 0.25,\ 0.51,\ 0.74,\ 0.90,\ 1.1$ and 1.2 bar m^{-1}, corresponding to the Reynolds numbers based on the channel depth $H = 33$ μm and average speed $Re = 0.03$–0.12. In all cases, the region imaged was about 17 mm downstream of the bend immediately downstream of the upstream reservoir (versus a total length of 28 mm for that particular straight section of channel, as shown in figure 1) to ensure fully developed flow. The fluid viscosity μ was taken to be that of water at the temperature of the exit reservoir, which was measured with a K-type thermocouple.

The fluorescent particles are illuminated by evanescent waves, which were generated by launching a $\lambda = 488$ nm beam from an argon-ion laser (Coherent Innova 90) with an output power of about 150 mW into the fused-silica microchannel 'sandwich' consisting of the bonded etched and unetched fused-silica pieces at the appropriate angle using a isosceles right-triangle prism. A second prism is used to couple the laser beam out of the fused-silica sandwich to minimize reflected and scattered light. In all cases, the TIR that generated the evanescent-wave illumination occurred at the interface between the unetched substrate and the working fluid; the near-wall flow region imaged is hence adjacent to the smoothest channel wall, which has a (r.m.s.) surface roughness of about 3 nm. The angle of incidence θ_i was estimated to be 72.3 ± 0.8 ° based upon the distance between the two TIR spots immediately adjacent to the imaged region and the thickness of the unetched substrate. The resultant penetration depth of the evanescent-wave illumination $z_p = 95.6 \pm 4.8$ nm.

The microchannel and prisms are mounted on the stage of an inverted epi-fluorescent microscope (Leica DMIRE2). The fluorescence from the polystyrene spheres excited by the evanescent-wave illumination is imaged at an effective overall

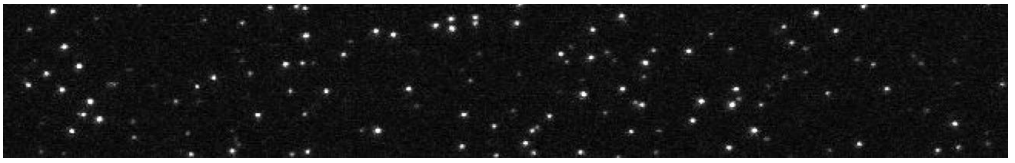

FIGURE 2. Typical experimental image for the Poiseuille flow of 2 mM NH_4HCO_3 through a bare channel for $\dot{\gamma} = 1410\ s^{-1}$.

magnification of 31.5 through a $63\times$ magnification and 0.7 numerical aperture objective (Leica PL Fluotar L), a longpass ($\lambda > 515$ nm) beamsplitter cube (Leica I3) that transmits only the red-shifted fluorescence, and a $0.5\times$ camera adaptor onto an electron multiplying CCD (EMCCD) camera (Photometrics Cascade 650). The images of the x–y plane of the flow (within about 400 nm of the wall, or for $z \leqslant 400$ nm) were then directly transferred from the CCD sensor to the RAM of a PC.

A pair of 0.8 ms wide pulses of evanescent-wave illumination separated by 1.5 ms was created by shuttering the continuous-wave laser beam with an acousto-optic modulator (IntraAction Corp. AOM-40). The fluorescence from the tracer particles was then imaged by the CCD as a pair of images with an exposure time of 0.8 ms separated by an interval $\Delta t = 1.5$ ms. Figure 2 shows a typical image for the Poiseuille flow of 2 mM NH_4HCO_3 through a bare fused-silica channel for $\dot{\gamma} = 1410\ s^{-1}$, or $Re = 0.09$. Two sequences, each consisting of 300 image pairs (= 600 images) with dimensions of 653 pixels $\times$ 100 pixels (154 μm $\times$ 24 μm), were acquired in each experimental run. Although each pair of images was acquired with an inter-image spacing of 1.5 ms, the time between image pairs varied due to limitations in the data-transfer rate from the CCD camera to the PC RAM. In other words, for a sequence of images numbered 1, 2, ..., 600, the spacing between images $2N - 1$ and $2N$ (where N is any integer from 1 to 300) was 1.5 ms, but the spacing between successive image pairs (i.e. between images $2N$ and $2N + 1$, where $N = [1 : 299]$) varied from 20 ms up to about 220 ms, giving a total image-acquisition time for the entire sequence of 33 ± 2 s. This variation in the time interval between image pairs should not affect the MnPTV results for this steady flow.

3. Near-wall particle distributions and velocities

After compensating all images for the nonlinear response of the EMCCD camera, an average 'background' image was calculated over all 600 image pairs. As shown in figure 3, a much larger number of the particle tracers adhere to the hydrophobic surface (only stationary particles should be visible in these time-averaged images). The increase in surface-attached particles is probably due to a reduction in the EDL repulsion between the wall and the negatively charged particles, since the hydrophobic coating should make the wall-surface charge less negative by reducing the number of exposed silanol groups. Independent streaming-potential measurements with 20 mM phosphate buffer at pH 6.8 estimated that the average wall zeta-potentials of the bare and hydrophobically coated channels were -3.5 and 0 mV, respectively. The increase in the number of surface-attached particles may also be due to an enhanced chemical affinity between the particles and the hydrophobic SAM.

Individual particle images were located with an in-house MATLAB code based on the approach of Crocker & Grier (1996). For each particle image, properties such as the (x, y) location of the centre, the radius, the maximum particle intensity or grey-scale value and the eccentricity, e, were calculated. Since non-circular particle images

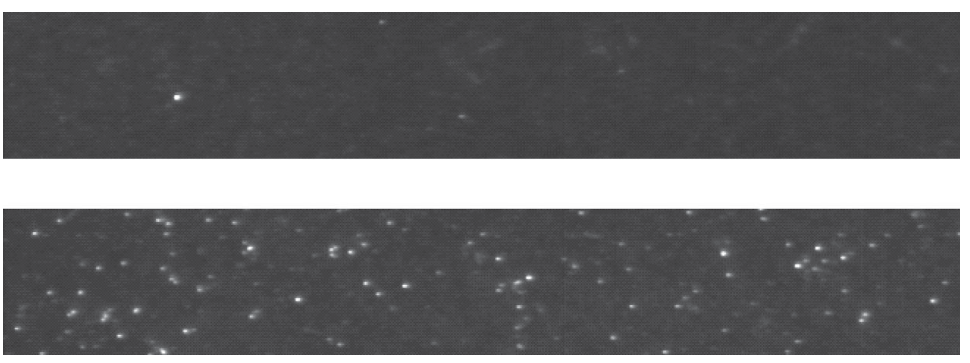

FIGURE 3. Average images of the near-wall flow for (*a*) bare and (*b*) hydrophobically coated channels calculated over the 600 image pairs obtained in a single experimental run. The images, have physical dimensions of 154 μm × 24 μm, and have been processed to enhance contrast.

were likely to be due to either aggregated particles or overlapping particle images, all particle images with $e > 0.1$ ($e = 0$ and 1 for a circle and line, respectively), typically about 10 % of the particle images, were removed. The images for Poiseuille flow through both the hydrophilic and hydrophobically coated channels were processed using the same procedures with one exception: for the hydrophobically coated case, the mean image was subtracted from each individual image to remove the background (i.e. the images of the surface-attached particles) before determining the actual particle displacements. Note that the actual particle image properties for the hydrophobic case were still calculated from the images before the background was removed.

The z-position of the centre of each particle of radius a was determined from the ratio of the maximum particle intensity (i.e. pixel grey-scale value) I_p to the maximum particle intensity for a particle attached to the surface I_p^0, or at $z = a$

$$z = a + z_p \ln\left\{\frac{I_p^0}{I_p}\right\}, \tag{3.1}$$

where the penetration depth was determined from known experimental parameters and I_p^0 was determined from images of tracers identical to those used in the Poiseuille flow experiments attached to the channel surface (with a 10 mM $CaCl_2$ solution) that were illuminated and imaged by the same apparatus as that used in the flow experiments Li & Yoda (2008). The uncertainty in the z-position of the particles, determined from the uncertainties in z_p and I_p^0, ranged from 17 nm for particles touching the wall to 23 nm for particles at $z = 350$ nm based on 95 % confidence intervals.

Figure 4 shows the resultant histogram of particle z-positions determined in each case over at least 8×10^4 particle images at $z < 350$ nm for both the (*a*) bare and (*b*) hydrophobically coated channels. In all cases, there are almost no particles at $z \leqslant 100$ nm, presumably due to electrokinetic interactions between the negatively charged polystyrene particles and the negatively charged wall. Shear-induced lift forces (Cherukat & McLaughlin 1994) should be negligible, given that the shear-based Reynolds numbers, Re_s, in these studies are much less than unity: $Re_s = a^2\dot{\gamma}/\nu < 6 \times 10^{-6}$.

The particle number density, c, reaches a maximum at around $z = 120$ nm, then decays to a roughly constant value within about 20 % of the nominal bulk value of 4.4×10^{16} m^{-3} for $z > 250$ nm. For a given channel, the particle distribution appears to

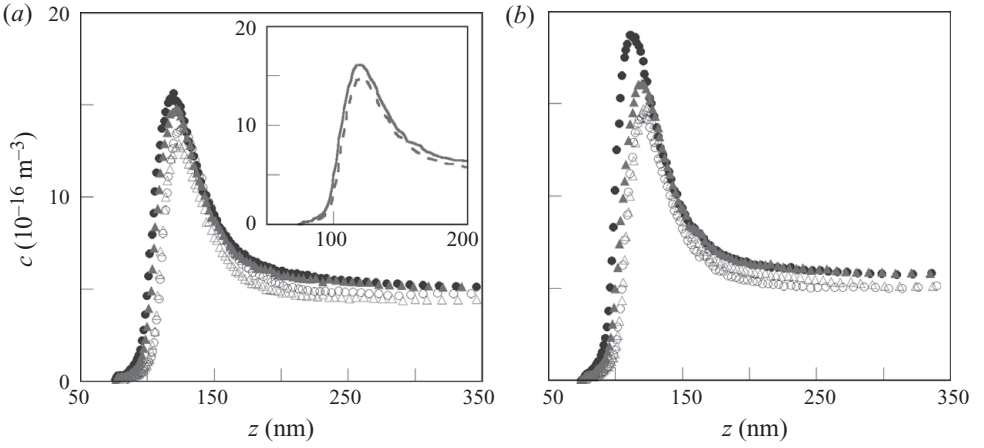

FIGURE 4. Particle number density c plotted as a function of the z-location of the particle centre (where $z = 0$ corresponds to the wall) for the Poiseuille flow of 2 mM (○) and 10 mM (●) CH_3COONH_4 and 2 mM (△) and 10 mM (▲) NH_4HCO_3 through (*a*) hydrophilic and (*b*) hydrophobically coated channels. The inset (note the expanded horizontal axis) compares the particle distributions for 10 mM NH_4HCO_3 solutions measured in the hydrophilic (dashed) and hydrophobic (solid line) channels. Both plots have the same vertical scale.

depend more strongly upon the electrolyte concentration (versus pH) of the working fluid: the two curves at the higher molar concentration cases (10 mM NH_4HCO_3 and 10 mM CH_3COONH_4, respectively) are shifted slightly towards the wall compared with the corresponding 2 mM cases. The inset in figure 4(*a*), which compares the curves for 10 mM NH_4HCO_3 flowing through the bare and coated channels, suggests that the particle distribution in the coated channel is slightly closer to the wall than the corresponding bare channel cases, in part because the hydrophobic coating changes the channel wall zeta-potential from −3.5 to 0 mV (for 20 mM phosphate buffer).

These histograms are assumed to be the steady-state distribution of the near-wall particles, since the data span more than 60 s of sampling time. Although not shown here, Brownian dynamics simulations using the Langevin equation indicate that the experimentally measured steady-state distribution is similar to the distribution of matched particles (where 'matched' implies that the particle is visible in both images of the pair) determined from the simulation data for the relatively short interval between the images in the pair $\Delta t = 1.5$ ms. Since the uncertainty (based on 95 % confidence intervals) in the z-position of each particle is a systematic error, the effect of this uncertainty will 'shift' the z-positions of the particles, and hence the particle distribution, by $\pm 17 - \pm 23$ nm. Given the large number of samples (as evident by the smoothness of the histogram), the error in the actual value of c should be negligible.

The particles were then divided, based on their intensities (see (3.1)), into three 'layers', each 100 nm thick:

(i) $50\ \text{nm} \leqslant z \leqslant 150\ \text{nm}$;
(ii) $150\ \text{nm} \leqslant z \leqslant 250\ \text{nm}$;
(iii) $250\ \text{nm} \leqslant z \leqslant 350\ \text{nm}$.

Each layer contains roughly one-third of the particles based on the particle distributions shown in figure 3. Previous Brownian dynamics simulations using the Fokker–Planck equation showed that Brownian effects could affect the accuracy of near-wall particle-based velocity data, and demonstrated that these effects became significant when the dimensionless time interval between the images within the pair

$\Omega^* = D_\infty \Delta t/(Z + 0.8a)^2$ exceeded 0.25 (Sadr *et al.* 2007). In this expression, D_∞ is the Stokes–Einstein diffusion coefficient in an unbounded flow and Z is the z-dimension of the imaged region. For particles of radius $a = 50$ nm in a layer with a z-extent $Z = 100$ nm, $\Omega^* = D_\infty \Delta t/(Z + 0.8a)^2 \approx 0.13$ for $\Delta t = 1.5$ ms, implying that such Brownian diffusion effects are not significant for these results.

The mean velocity in each of the three layers was then determined from data obtained over the 600 image pairs in each run using the particle-tracking approach of Baek & Lee (1996). PTV was used in lieu of correlation-based PIV because the non-uniform intensity of evanescent-wave illumination can bias correlation-based approaches, as shown by Sadr *et al.* (2007).

After obtaining the mean velocity component tangential to the wall, the z-positions of these velocities must be determined. The results shown in figure 4 clearly demonstrate that the tracers non-uniformly sample the fluid velocity field. The average z-position for each of the three layers (I, II, III) is, therefore, calculated from the particle number density profiles $c(z)$ shown in this figure where the particle concentration-weighted average z-position is calculated as follows:

$$\bar{z} = \frac{\int_{Z_L}^{Z_U} c(z) z \, \mathrm{d}z}{\int_{Z_L}^{Z_U} c(z) \, \mathrm{d}z}, \tag{3.2}$$

for a layer that spans a range of z-positions $Z_L \leqslant z \leqslant Z_U$. We emphasize that MnPTV, unlike other tracer-based velocimetry techniques, directly measures and accounts for non-uniform particle distributions when determining the z-position of the velocity in each layer. The z-position of the MnPTV result for layer I nearest the wall, $\bar{z}_I$, was most affected by the non-uniform particle distribution. For the four working fluids and two types of channels, the values of $\bar{z}_I$ varied from 121–128 nm, versus the geometric centre of layer I, $z_{CI} = 100$ nm.

The slope of the MnPTV data determined by linear regression, or the experimentally determined shear rate $\dot{\gamma}_M$, was compared with the 'expected' value from analytical predictions of the velocity. Given that the aspect ratio of the channel cross-section exceeds 16, the expected mean velocities in the three layers are determined from the exact solution for two-dimensional Poiseuille flow between infinite parallel plates separated by a distance $H = 33\,\mu$m (solid line)

$$u(z) = \frac{H^2}{2\mu} \frac{\mathrm{d}p}{\mathrm{d}x} \left[\frac{z}{H} \left(1 - \frac{z}{H} \right) \right], \tag{3.3}$$

using the measured pressure gradient $\mathrm{d}p/\mathrm{d}x$ and viscosity of the working fluid μ. Note that (3.3) assumes that the no-slip condition holds, i.e. the fluid velocity at the wall ($z = 0$) is zero. The expected shear rate $\dot{\gamma}$ was then obtained from linear regression of $u(z)$ for $z < 400$ nm.

To compare the MnPTV results, which are, strictly speaking, particle (versus fluid) velocities, with the velocity profile $u(z)$ given in (3.3), we should first consider the effect of particle–fluid 'slip' due to the rotation of the particle in the shear-dominated flow near the wall. The classic paper by Goldman, Cox & Brenner (1967), who determined the velocity of a sphere near a solid planar wall convected by simple shear flow with shear rate $\dot{\gamma}$, gives the dimensionless particle velocity $U/(\dot{\gamma} z)$, as a function of the dimensionless separation distance z/a and $(z - a)/a$ in their tables 2 and 3, respectively. Based on this correction, however, the ratio between the particle

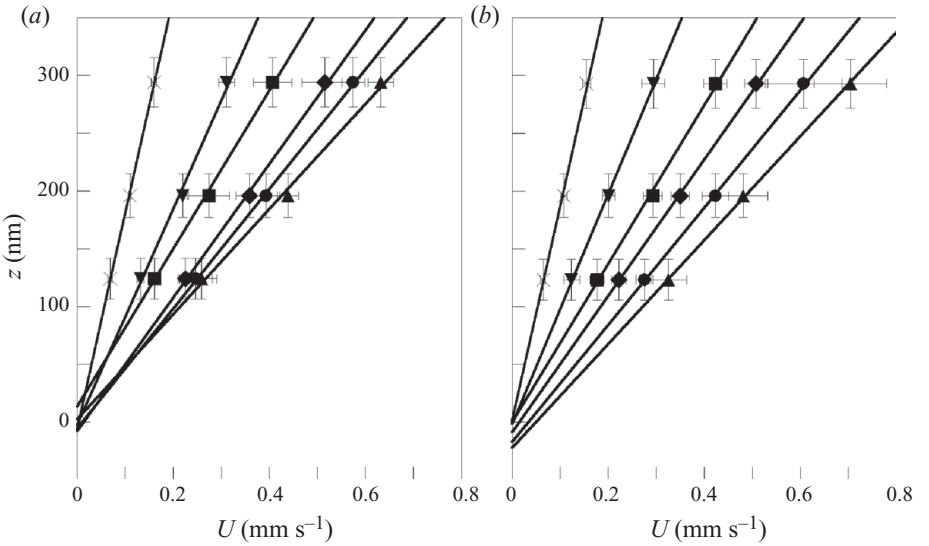

FIGURE 5. Average velocities U obtained using MnPTV (points) as a function of the wall-normal distance z in the three layers for the Poiseuille flow of 10 mM NH_4HCO_3 at six different shear rates in (*a*) hydrophilic and (*b*) hydrophobically coated fused-silica channels; both graphs have the same vertical scale. The lines denote weighted least-squares curve-fits of the MnPTV results.

and the fluid velocities rapidly approaches unity as z/a increases – for $z/a > 2$, 'the lag is less than about 3 %' (Goldman *et al.* 1967), and the lag is about 2 % when $z/a = 2.4$ or $z = 120$ nm. Given that the z-position of the MnPTV data nearest the wall $\bar{z}_I > 120$ nm in all cases, this lag, which is effectively the maximum error in the fluid velocity due to the particle rotation is much less than the experimental uncertainty in the velocity data, with average 95 % confidence intervals of about 9 %. The MnPTV results presented here are, therefore, directly compared with the exact solution for $u(z)$ given in (3.3).

Figure 5 shows velocities measured using MnPTV, U, for the Poiseuille flow of 10 mM NH_4HCO_3 (pH 7.8) through (*a*) bare and (*b*) hydrophobically coated fused-silica microchannels at six different shear rates (points), as well as a linear curve-fit of the three data points at each shear rate (line). The six cases shown in figure 5(*a*) correspond to analytically determined shear rates $\dot{\gamma}$ of 491 (×), 983 (▼), 1412 (■), 1720 (◆), 2029 (●) and 2255 (▲) s^{-1}; those shown in figure 5(*b*) correspond to $\dot{\gamma} = 487$ (×), 961 (▼), 1398 (■), 1706 (◆), 2025 (●) and 2256 (▲) s^{-1}. The small differences in shear rate for the two different channels are mainly due to slight variations in the driving pressure gradient and fluid temperature (and hence viscosity). Each MnPTV data point is placed at the average z-position $\bar{z}$ sampled by the particles in that layer (see (3.2)), and represents the velocities averaged over five independent experiments under identical conditions. The horizontal error bars represent 95 % confidence intervals (i.e. twice the standard deviations) for the MnPTV estimates of U, while the vertical error bars represent 95 % confidence intervals for the particle position at the z-location corresponding to that value of $\bar{z}$, which were 18, 19 and 21 nm for layers I, II and III, respectively.

The solid lines in figure 5 are the results from linear regression of the MnPTV data using a MATLAB routine for a weighted least-squares curve-fit that considers the

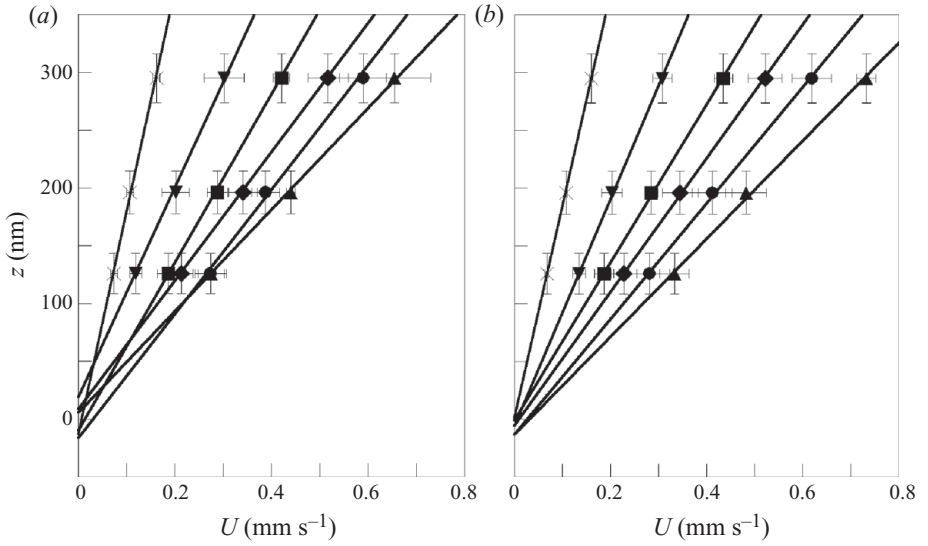

FIGURE 6. Same as figure 5, but for the flow of 2 mM CH_3COONH_4 through (*a*) hydrophilic and (*b*) hydrophobically coated channels. Again, both graphs have the same vertical scale.

standard deviations in z and U for each of the three points (Krystek & Anton 2007). The maximum and minimum discrepancies between the shear rate $\dot{\gamma}_M$ obtained from these MnPTV data (i.e. the slope of the solid lines) and $\dot{\gamma}$ are 11 % (for $\dot{\gamma} = 487$ s^{-1} hydrophobic case) and 0.6 % (for the $\dot{\gamma} = 1720$ s^{-1} hydrophilic case), respectively; the mean discrepancy for this fluid averaged over six different shear rates and two different channels is 4.5 %.

Figure 6 shows similar results for the Poiseuille flow of 2 mM CH_3COONH_4 (pH 6.2) through (*a*) bare and (*b*) hydrophobically coated fused-silica microchannels. The six analytical shear rates for the hydrophilic case are $\dot{\gamma} = 493\,(\times)$, 972 (▼), 1409 (■), 1735 (◆), 2026 (●) and 2260 (▲) s^{-1}; those for the hydrophobic case are $\dot{\gamma} = 493\,(\times)$, 974 (▼), 1409 (■), 1708 (◆), 2025 (●) and 2257 (▼) s^{-1}. The maximum and minimum discrepancies between the shear rate $\dot{\gamma}_M$ obtained from these MnPTV data and $\dot{\gamma}$ are 13 % (for $\dot{\gamma} = 972$ s^{-1} hydrophilic case) and 0.6 % (for $\dot{\gamma} = 2260$ s^{-1} hydrophilic case), respectively; the discrepancy for this fluid averaged over all 12 cases is 5.0 %. Although not shown here, the results for 2 mM NH_4HCO_3 and 10 mM CH_3COONH_4 are qualitatively similar to those shown in figures 5 and 6, respectively. The average discrepancy between $\dot{\gamma}_M$ and $\dot{\gamma}$ for the six shear rates for all four working fluids was 5.1 % for the hydrophilic cases and 4.6 % for the hydrophobic cases.

The slip lengths for these data can then be found by extrapolating the linear curve-fits shown in figures 5 and 6 to the z-position where $U = 0$. Figure 7 shows these slip lengths b as a function of the analytically predicted shear rate for the (*a*) hydrophilic and (*b*) hydrophobically coated channels (negative values of slip length imply that $U = 0$ within the fluid). The error bars denote the maximum standard deviation in the slip lengths determined from the uncertainties in the curve-fit based upon the standard deviations in U and z. The standard deviations in the slip lengths range from 18 to 25 nm for the hydrophilic cases and from 18 to 40 nm for the hydrophobic cases. The maximum value of b is 18 ± 23 nm (10 mM CH_3COONH_4 at $\dot{\gamma} = 1414$ s^{-1})

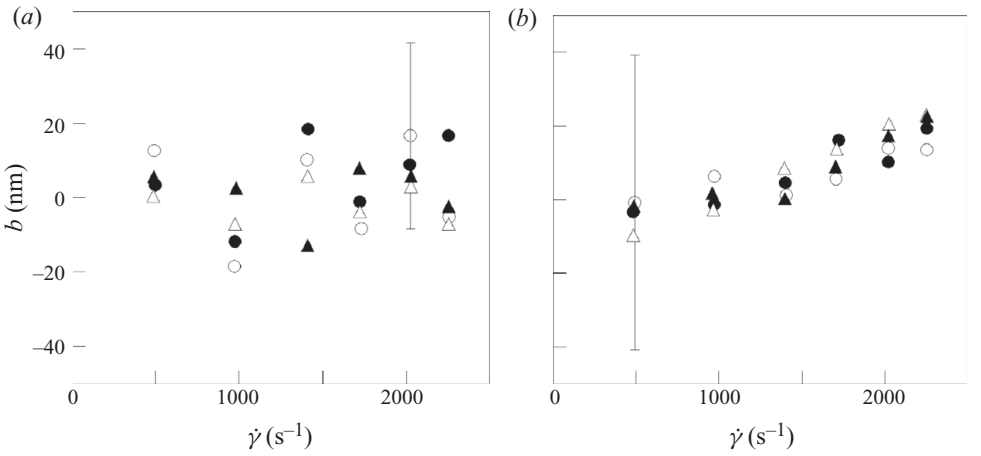

FIGURE 7. Slip lengths b as a function of shear rate $\dot{\gamma}$ for the Poiseuille flow of 2 mM (○) and 10 mM (●) CH_3COONH_4 and 2 mM (△) and 10 mM (▲) NH_4HCO_3 through (*a*) hydrophilic and (*b*) hydrophobically coated channels; both graphs have the same vertical scale. The error bars denote the maximum standard deviations in the slip lengths of (*a*) 25 nm and (*b*) 40 nm.

for the hydrophilic cases and 23 ± 22 nm (2 mM NH_4HCO_3 at $\dot{\gamma} = 2251$ s^{-1}) for the hydrophobic cases.

Despite significant scatter, all the slip lengths are zero within their standard deviations except for one case, where $b = 23 \pm 22$ nm for the 2 mM NH_4HCO_3 hydrophobic case at $\dot{\gamma} = 2251$ s^{-1}. There appears to be less scatter in the slip lengths at a given shear rate for the hydrophobically coated channel, however, and unlike the hydrophilic case, b seems to increase (slightly) as $\dot{\gamma}$ increases. Several studies determining slip lengths from a variety of different techniques, including tracer-based velocimetry (Huang *et al.* 2006), volume-flow-rate measurements (Choi *et al.* 2003) and AFM-based force data (Neto *et al.* 2003), have also reported slip lengths that increase with $\dot{\gamma}$, albeit at much higher shear rates: 8000 s^{-1} for Neto *et al.* (2003) and 10^5 s^{-1} for Choi *et al.* (2003), versus the maximum shear rate studied here of about 2300 s^{-1}.

The standard deviation in b for these MnPTV results of 18–25 nm for the hydrophilic channel and 18–40 nm for the hydrophobically coated channel are comparable to those reported in other studies. Joseph & Tabeling (2005) reported an uncertainty of about 100 nm, based apparently upon 95 % confidence intervals, in their slip-length estimates. Schmatko *et al.* (2005) gave an uncertainty of about 50 nm. Lasne *et al.* (2008) reported an uncertainty of 15 and 10 nm in their values for b from evanescent wave-based PIV of 20 and 40 nm diameter tracers and fluorescent molecules with a maximum dimension of 1 nm or less, respectively. Finally, Joly *et al.* (2006) reported an uncertainty of 5 nm for their slip-length results obtained from measuring 'thermal' (i.e. Brownian) near-wall diffusion times using FCS.

The results given in figure 7 suggest that neither the ionic strength nor the pH of the working fluid has a significant effect upon slip length, at least for the cases studied here. This result is in agreement with Huang & Breuer (2007), who reported that the slip length was essentially constant over a 10-fold change in ionic strength for aqueous NaCl solutions (versus the fivefold change considered here).

The 'more organized' nature of the slip-length results for the hydrophobic cases suggests that the hydrophilic and hydrophobically coated cases may have inherent differences. Assuming that the geometric variations between two channels, which were etched on the same wafer and hence subject to the same etching process, are negligible, and given that the experimental procedures and image processing procedures were identical (with the exception of the step for removing 'background' stationary particles) for these two cases, the major difference between the hydrophilic and hydrophobic cases appears to be the greater number of particles that adhere to the hydrophobic surface. Although we are not aware of any other reports of this phenomenon, the hydrophobic OTS SAM coatings for the fused-silica microchannels studied here are similar to those studied by several other groups, including Tretheway & Meinhart (2004), Huang *et al.* (2006) and Huang & Breuer (2007), suggesting that more particles may have adhered to their hydrophobically coated surfaces as well.

Despite the increase in surface-attached particles in the hydrophobic (versus the hydrophilic) case, we emphasize that these stationary particles occupy a very small fraction of the surface, with projected area of not more than 0.01 % of the total area of the image itself, and that the average inter-particle distance between the attached particles exceeds $50a$. Nevertheless, the presence of these particles could change the nature of the flow itself by increasing surface roughness, and perhaps more importantly, introducing spatial non-uniformities in both the surface hydrophobicity and charge. Pit *et al.* (2000), who measured slip lengths in hexane flowing over bare and methylated sapphire surfaces, reported that increasing the density of methyl groups on the surface (corresponding to a less wetting surface) was associated with an increase in slip length for a wide variety of hydrophobic coatings, including OTS and perfluorodecane trichlorosilane (FTS). The slip length for what they termed a 'slightly incomplete OTS monolayer' was 100 ± 50 nm, while $b = 400 \pm 100$ nm for a 'dense OTS surface'. The stationary particles could also affect the accuracy of the MnPTV result by distorting the evanescent-wave illumination (the refractive index of polystyrene is about 1.55), thereby affecting the exponential decay of the illumination intensity. The z-location of each particle based on (3.1) – and hence $\bar{z}$, the average z-position of the velocities sampled by the colloidal tracers – may, therefore, be less accurate for the hydrophobic (versus hydrophilic) cases.

On a related note, the non-uniform distribution of tracers in the near-wall region has a marked effect on the accuracy of these velocity data. Figure 8 illustrates this effect for the Poiseuille flow of 10 mM NH_4HCO_3 through (a) hydrophilic and (b) hydrophobically coated channels. For the hydrophilic case, a subset of the results from figure 5(a) at three (versus six) shear rates $\dot{\gamma} = 983$ (▼), 1720 (◆) and 2255 (▲) s^{-1} corrected for the non-uniform distribution (filled symbols) are plotted here, along with linear curve-fits to these corrected MnPTV data (solid lines); for the hydrophobic case, $\dot{\gamma} =$ 961 (▼), 1706 (◆) and 2256 (▲) s^{-1}. These results are compared with the same velocity results placed at the z-position corresponding to the geometric centre of the three layers I, II and III, or z-values of 100, 200 and 300 nm, respectively (open symbols), and linear curve-fits to these 'uncorrected' MnPTV data (dashed lines). The biggest 'shift' in the z-position of the velocity data point is for layer I, or the layer nearest the wall. Note that the curve-fits shown here take into account the uncertainties in these data, specifically the standard deviations in U and the uncertainties of 8.5, 9.5 and 11 nm at $z = 100$, 200 and 300 nm, respectively, which correspond to the standard deviations in the particle position at that value of z.

For the results shown here, shifting the velocity result for layer I towards the wall by no more than 24 nm increases the slip length by 40–51 nm, as shown in table 1, and

Hydrophilic

$\dot{\gamma}$ (s^{-1})	$\dot{\gamma}_M$ (s^{-1})	$\dot{\gamma}_U$ (s^{-1})	b (nm)	b_U (nm)
983	1070	893	2.6	47
1720	1730	1423	8.0	57
2255	2198	1864	−2.3	38

Hydrophobically coated

$\dot{\gamma}$ (s^{-1})	$\dot{\gamma}_M$ (s^{-1})	$\dot{\gamma}_U$ (s^{-1})	b (nm)	b_U (nm)
961	1004	841	1.8	44
1706	1692	1406	9.0	55
2256	2222	1834	23	74

TABLE 1. Comparison of shear rates $\dot{\gamma}_M$ and $\dot{\gamma}_U$ and slip-length values b and b_U derived from MnPTV results corrected for the non-uniform tracer distribution and assuming uniformly distributed tracers, respectively, for the three different shear rates shown in figure 8. The MnPTV results for shear rate are compared with that predicted by the analytical solution $\dot{\gamma}$.

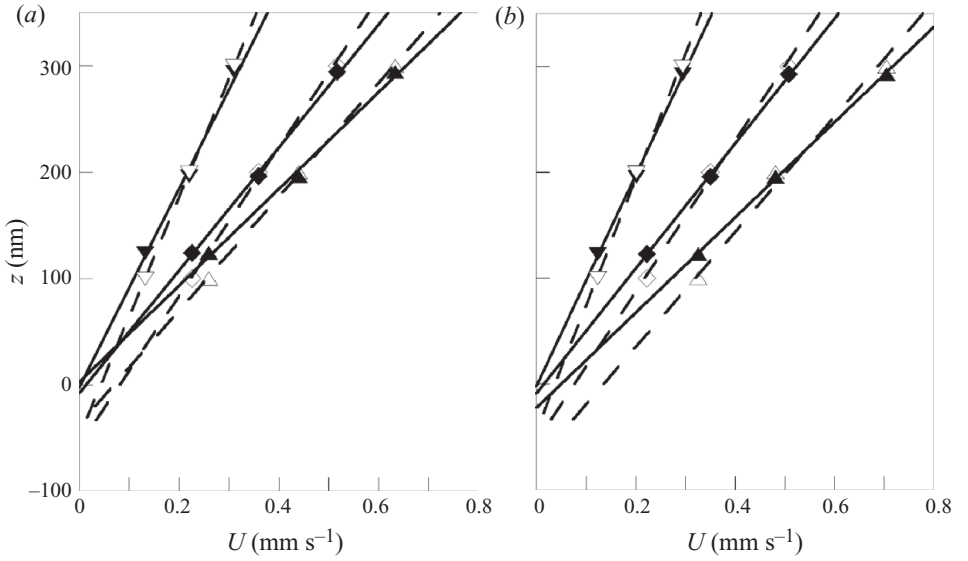

FIGURE 8. Comparison of MnPTV results corrected for the non-uniform near-wall tracer distribution (filled symbols and solid lines) and placed at z-positions, assuming a uniform tracer distribution (open symbols and dashed lines) for the flow of 10 mM NH_4HCO_3 through (*a*) hydrophilic channels at shear rates $\dot{\gamma} = 983$ (▼), 1720 (◆) and 2255 (▲) s^{-1} and (*b*) hydrophobically coated channels at $\dot{\gamma} = 961$ (▼), 1706 (◆) and 2256 (▲) s^{-1}. Both plots have the same vertical scale.

gives slip length values b_U as great as 74 nm. Not accounting for the non-uniform distribution of the near-wall tracers also gives a significantly greater discrepancy between the shear rates obtained from the MnPTV data; the average discrepancy for the shear rates obtained from the MnPTV results assuming uniformly distributed tracers $\dot{\gamma}_U$ and those predicted by the analytical solution $\dot{\gamma}$ is 15 % over these three

different shear rates for the hydrophilic and hydrophobic channels versus an average discrepancy of 3.3 % between $\dot{\gamma}_M$ and $\dot{\gamma}$.

The Derjaguin–Landau and Verwey–Overbeek (DLVO) theory, which describes the interaction between a colloidal tracer suspended in a density-matched conducting fluid and a charged planar surface due to their (usually repulsive) EDL interactions and (usually attractive) van der Waals interactions, predicts that the near-wall distribution of colloidal tracers will be non-uniform in nearly all cases (see e.g. Israelachvili 1992). Given that the majority of studies finding non-zero slip lengths report $b = O(100\text{ nm})$, it is likely that the tracer-based estimates of near-wall velocities for techniques that can resolve velocities within $O(100\text{ nm})$ of the wall involve non-uniformly distributed tracers. As illustrated by these MnPTV data for 100 nm PS spheres, accounting for this non-uniform distribution significantly improves the accuracy of the near-wall tracer-based velocimetry results and reduces the slip lengths estimated by using this local method. This technique is, to our knowledge, the only near-wall velocimetry technique that directly measures and corrects for the non-uniform distribution of near-wall tracers.

4. Conclusion

Slip lengths were estimated for the steady and creeping Poiseuille flow through 33 μm deep naturally hydrophilic and hydrophobically coated fused-silica microchannels using a local method. The MnPTV technique used in these studies tracks 100 nm fluorescent tracers illuminated by evanescent waves to determine tangential velocities at three different distances from the wall (based upon tracer-image intensity) within about 400 nm of the wall. The slip length, determined from the intercept of a linear curve-fit to three near-wall velocity data points at shear rates ranging from about 500 to 2600 s^{-1}, was at most 18 ± 23 nm and 23 ± 22 nm for the hydrophilic and hydrophobic cases, respectively. If these estimates of slip length are valid, the results suggest that the effects of slip will only be significant for flows with overall dimensions well below 1 μm, and that the no-slip boundary condition is a reasonable approximation for the flows of Newtonian liquids through channels with dimensions exceeding 1 μm.

Four aqueous monovalent electrolyte solutions at different pH values and ionic strengths were studied. Neither solution pH nor ionic strength appeared to affect the slip lengths, at least for the pH and ionic strength ranges (6.2–7.8 mM and 2–10 mM salt molar concentrations, respectively) studied here. As further validation of these data, the shear rates calculated from the slope of these linear curve-fits were within 5 % on average of the values predicted by a linear curve-fit to the analytical solution for Poiseuille flow between parallel plates.

As predicted by DLVO theory from surface science, the distribution of the 100 nm tracers is highly non-uniform, with almost no particles within a diameter of the wall, due presumably to repulsive electric double layer interactions between the negatively charged particles and the negatively charged fused-silica surface. Measuring and accounting for this non-uniform distribution, which changes the average wall-normal distance for the velocities sampled by the particles in each layer, significantly reduces estimates of slip length and improves the accuracy of the estimated shear rates. In these data, moving the velocity data point nearest the wall less than 24 nm farther away from the wall increased the slip length by as much as 51 nm.

The range of slip lengths were similar between the hydrophilic and hydrophobically coated cases. However, at a given shear rate the slip lengths for the hydrophobically

coated channels have significantly less 'scatter' than the comparable hydrophilic case, and appear to increase as shear rate increases (see figure 7). The standard deviation in the slip lengths obtained from the MnPTV data is also slightly greater for the hydrophobically coated channel cases. The discrepancy in the relationship between slip length and shear rate between the naturally hydrophilic (uncoated) fused-silica channels and similar channels coated with a hydrophobic self-assembled monolayer may be due in part to the larger number of tracer particles that adsorb onto the channel wall for the hydrophobic case. These surface-attached particles increase the surface roughness and probably introduce local variations in the surface charge and hydrophobicity of the channel 'wall'.

This work was supported by NSF grant CBET-0828782 from the Particulate and Multiphase Processes and Fluid Dynamics Programs. The authors thank J. P. Alarie and Professor J. M. Ramsey from the Department of Chemistry at the University of North Carolina for fabricating the fused-silica microchannels, and G. S. Philibert and Professor S. V. Olesik from the Department of Chemistry at the Ohio State University for providing estimates of the wall zeta-potential for these microchannels. The MATLAB routine used for the linear regression, wtls_line.m, submitted by M. Anton, was obtained from the MATLAB Central File Exchange (http: //www.mathworks.com/matlabcentral/fileexchange/).

REFERENCES

Baek, S. J. & Lee, S. J. 1996 A new two-frame particle tracking algorithm using match probability. *Exp. Fluids* **22** (1), 23–32.

Batchelor, G. K. 1967 *An Introduction to Fluid Mechanics*. Cambridge University Press.

Bocquet, L. & Barrat, J. L. 2007 Flow boundary conditions from nano- to micro-scales. *Soft Matter* **3** (6), 685–693.

Bonaccurso, E., Butt, H. J. & Craig, V. S. J. 2003 Surface roughness and hydrodynamic boundary slip of a Newtonian fluid in a completely wetting system. *Phys. Rev. Lett.* **90** (14), 144501.

Bonaccurso, E., Kappl, M. & Butt, H. J. 2002 Hydrodynamic force measurements: boundary slip of water on hydrophilic surfaces and electrokinetic effects. *Phys. Rev. Lett.* **88** (7), 076103.

Breedveld, V., Van den Ende, D., Tripathi, A. & Acrivos, A. 1998 The measurement of the shear-induced particle and fluid tracer diffusivities in concentrated suspensions by a novel method. *J. Fluid Mech.* **375**, 297–318.

Cheng, J. T. & Giordano, N. 2002 Fluid flow through nanometer-scale channels. *Phys. Rev.* E **65**, 031206.

Cherukat, P. & McLaughlin, J. B. 1994 The inertial lift on a rigid sphere in a linear shear flow field near a flat wall. *J. Fluid Mech.* **263**, 1–18.

Cho, J. H. J., Law, B. M. & Rieutord, F. 2004 Dipole-dependent slip of Newtonian liquids at smooth solid hydrophobic surfaces. *Phys. Rev. Lett.* **92** (16), 166102.

Choi, C. H., Westin, K. J. A. & Breuer, K. S. 2003 Apparent slip flows in hydrophilic and hydrophobic microchannels. *Phys. Fluids* **15** (10), 2897–2902.

Cottin-Bizonne, C., Steinberger, A., Cross, B., Raccurt, O. & Charlaix, E. 2008 Nanohydrodynamics: the intrinsic flow boundary condition on smooth surfaces. *Langmuir* **24** (4), 1165–1172.

Crocker, J. C. & Grier, D. G. 1996 Methods of digital video microscopy for colloidal studies. *J. Colloid Interface Sci.* **179** (1), 298–310.

Goldman, A. J., Cox, R. G. & Brenner, H. 1967 Slow viscous motion of a sphere parallel to a plane wall. Part II. Couette flow. *Chem. Engng Sci.* **22**, 653–660.

Guasto, J. S., Huang, P. & Breuer, K. S. 2006 Statistical particle tracking velocimetry using molecular and quantum dot tracer particles. *Exp. Fluids* **41**, 869–880.

Henry, C. L., Neto, C., Evans, D. R., Biggs, S. & Craig, V. S. J. 2004 The effect of surfactant adsorption on liquid boundary slippage. *Physica* A **339** (1–2), 60–65.

Honig, C. D. F. & Ducker, W. A. 2007 No-slip hydrodynamic boundary condition for hydrophilic particles. *Phys. Rev. Lett.* **98** (2), 028305.

Huang, P. & Breuer, K. S. 2007 Direct measurement of slip length in electrolyte solutions. *Phys. Fluids* **19** (2), 028104.

Huang, P., Guasto, J. S. & Breuer, K. S. 2006 Direct measurement of slip velocities using three-dimensional total internal reflection velocimetry. *J. Fluid Mech.* **566**, 447–464.

Israelachvili, J. N. 1992 *Intermolecular and Surface Forces*. Academic Press.

Joly, L., Ybert, C. & Bocquet, L. 2006 Probing the nanohydrodynamics at liquid–solid interfaces using thermal motion. *Phys. Rev. Lett.* **96** (4), 046101.

Joseph, P. & Tabeling, P. 2005 Direct measurement of the apparent slip length. *Phys. Rev.* E **71**, 035303(R).

Kanda, K., Ogata, S., Jingu, K. & Yang, M. 2007 Measurement of particle distribution in microchannel flow using a 3D-TIRFM technique. *J. Vis. Japan* **10** (2), 207–215.

Krystek, M. & Anton, M. 2007 A weighted total least-squares algorithm for fitting a straight line. *Meas. Sci. Technol.* **18**, 3348–3442.

Lasne, D., Maali, A., Amarouchene, Y., Cognet, L., Lounis, B. & Kellay, H. 2008 Velocity profiles of water flowing past solid glass surfaces using fluorescent nanoparticles and molecules as velocity probes. *Phys. Rev. Lett.* **100** (21), 214502.

Lauga, E., Brenner, M. P. & Stone, H. A. 2005 Microfluidics: the no-slip boundary condition. In *Handbook of Experimental Fluid Dynamics* (ed. C. Tropea, J. Foss & A. Yarin), pp. 1219–1240. Springer.

Li, H. F. 2008 An evanescent-wave-based particle image velocimetry technique. PhD thesis, Georgia Institute of Technology, Atlanta, GA.

Li, H. F., Sadr, R. & Yoda, M. 2006 Multilayer nano-particle image velocimetry. *Exp. Fluids* **41** (2), 185–194.

Li, H. F. & Yoda, M. 2008 Multilayer nano-particle image velocimetry (MnPIV) in microscale Poiseuille flows. *Meas. Sci. Technol.* **19** (7), 075402.

Lumma, D., Best, A., Gansen, A., Feuillebois, F., Radler, J. O. & Vinogradova, O. I. 2003 Flow profile near a wall measured by double-focus fluorescence cross-correlation. *Phys. Rev.* E **67**, 056313.

Maccarini, M. 2007 Water at solid surfaces: a review of selected theoretical aspects and experiments on the subject. *Biointerphases* **2** (3), MR1–MR15.

Navier, C. L. M. H. 1823 On the laws of movement of fluids. *Mem. de l'Acad. roy. des Sciences de l'inst. de France* **6**, 389–440.

Neto, C., Craig, V. S. J. & Williams, D. R. M. 2003 Evidence of shear-dependent boundary slip in Newtonian liquids. *Eur. Phys. J.* E **12**, S71–S74.

Neto, C., Evans, D. R., Bonaccurso, E., Butt, H. J. & Craig, V. S. J. 2005 Boundary slip in Newtonian liquids: a review of experimental studies. *Rep. Prog. Phys.* **68** (12), 2859–2897.

Pit, R., Hervet, H. & Leger, L. 2000 Direct experimental evidence of slip in hexadecane: solid interfaces. *Phys. Rev. Lett.* **85** (5), 980–983.

Priezjev, N. V. & Troian, S. M. 2006 Influence of periodic wall roughness on the slip behaviour at liquid/solid interfaces: molecular-scale simulations versus continuum predictions. *J. Fluid Mech.* **554**, 25–46.

Sadr, R., Hohenegger, C., Li, H. F., Mucha, P. J. & Yoda, M. 2007 Diffusion-induced bias in near-wall velocimetry. *J. Fluid Mech.* **577**, 443–456.

Sbragaglia, M., Benzi, R., Biferale, L., Succi, S. & Toschi, F. 2006 Surface roughness-hydrophobicity coupling in microchannel and nanochannel flows. *Phys. Rev. Lett.* **97** (20), 204503.

Schmatko, T., Hervet, H. & Leger, L. 2005 Friction and slip at simple fluid–solid interfaces: the roles of the molecular shape and the solid–liquid interaction. *Phys. Rev. Lett.* **94** (24), 244501.

Schmatko, T., Hervet, H. & Leger, L. 2006 Effect of nanometric-scale roughness on slip at the wall of simple fluids. *Langmuir* **22** (16), 6843–6850.

Thompson, P. A. & Troian, S. M. 1997 A general boundary condition for liquid flow at solid surfaces. *Nature* **389** (6649), 360–362.

Tretheway, D. C. & Meinhart, C. D. 2002 Apparent fluid slip at hydrophobic microchannel walls. *Phys. Fluids* **14** (3), L9–L12.

Tretheway, D. C. & Meinhart, C. D. 2004 A generating mechanism for apparent fluid slip in hydrophobic microchannels. *Phys. Fluids* **16** (5), 1509–1515.

Vinogradova, O. I., Koynov, K., Best, A. & Feuillebois, F. 2009 Direct measurements of hydrophobic slippage using double-focus fluorescence cross-correlation. *Phys. Rev. Lett.* **102**, 118302.

Yi, Y. W., Robinson, H. G., Knappe, S., Maclennan, J. E., Jones, C. D., Zhu, C., Clark, N. A. & Kitching, J. 2008 Method for characterizing self-assembled monolayers as antirelaxation wall coatings for alkali vapor cells. *J. Appl. Phys.* **104**, 023534.

Zhu, Y. & Granick, S. 2001 Rate-dependent slip of Newtonian liquid at smooth surfaces. *Phys. Rev. Lett.* **87** (9), 096105.

Zhu, Y. & Granick, S. 2002 Limits of the hydrodynamic no-slip boundary condition. *Phys. Rev. Lett.* **88** (10), 106102.